

RESEARCH ARTICLE | NOVEMBER 16 2023

The effect of shape, polydispersity, charge, and fraction of crystallite bundles on the cholesteric pitch of cellulose nanocrystal suspensions

Tor Sewring  ; Marjolein Dijkstra  



J. Chem. Phys. 159, 194902 (2023)

<https://doi.org/10.1063/5.0167362>



View
Online



Export
Citation

CrossMark

The Journal of Chemical Physics

Special Topic: Algorithms and Software for Open Quantum System Dynamics

Submit Today

The effect of shape, polydispersity, charge, and fraction of crystallite bundles on the cholesteric pitch of cellulose nanocrystal suspensions

Cite as: J. Chem. Phys. 159, 194902 (2023); doi: 10.1063/5.0167362

Submitted: 12 July 2023 • Accepted: 17 October 2023 •

Published Online: 16 November 2023



Tor Sewring¹ and Marjolein Dijkstra^{1,2,a)}

AFFILIATIONS

¹Soft Condensed Matter & Biophysics, Debye Institute for Nanomaterials Science, Utrecht University, Princetonplein 1, 3584 CC Utrecht, The Netherlands

²International Institute for Sustainability with Knotted Chiral Meta Matter (WPI-SKCM²), Hiroshima University, 1-3-1 Kagamiyama, Higashi-Hiroshima, Hiroshima 739-8526, Japan

^{a)}Author to whom correspondence should be addressed: m.dijkstra@uu.nl

ABSTRACT

Using Onsager–Straley’s second-virial theory, we investigate the cholesteric pitch of cellulose nanocrystal (CNC) suspensions. We model the CNCs as hard chiral bundles of microfibrils and examine the effect of the shape of these chiral bundles, characterized by aspect ratio and chirality, on the cholesteric pitch. Additionally, we explore the impact of length polydispersity and surface charge on the cholesteric phase of CNCs. Furthermore, we consider binary mixtures of twisted bundles and achiral primary crystallites to provide a more realistic representation of CNC suspensions. Our findings reveal that the degree of bundle twisting significantly affects the helical twisting of the cholesteric phase. We also observe that the average particle length and length polydispersity have substantial effects on strongly twisted bundles but minimal effects on weakly twisted ones. Finally, our study indicates that as the range of electrostatic interactions increases, the transfer of chirality from the microscopic to macroscopic length scales becomes masked, resulting in an increase in the cholesteric pitch. In the case of binary mixtures, the bundles act as chiral dopants, and an increasing fraction of bundles progressively enhances the helical twisting of the cholesteric phase.

Published under an exclusive license by AIP Publishing. <https://doi.org/10.1063/5.0167362>

I. INTRODUCTION

Over the past two decades, cellulose nanocrystals (CNCs) have attracted significant attention as a renewable source for various applications, including photonic materials.¹ When immersed in a solvent, these anisotropic colloidal particles self-assemble into cholesteric phases at sufficiently high concentrations,² and it is worth noting that the pitch of these cholesteric phases decreases as the concentration increases.³

Experimental systems using CNCs typically employ water as a solvent, and the surfaces of the CNCs are charged with acidic functional groups. These groups become ionized during the production process, resulting in a negative electric charge on the particles, which aids in stabilizing the dispersion. The charged groups grafted onto the CNC surfaces often include anionic sulfate half-esters (OSO_3^-),

which are formed through the hydrolysis of cellulose derived from wood or cotton using sulfuric acid. This hydrolysis process dissolves the disordered regions of the cellulose fibrils while preserving the crystalline parts, ultimately leading to the formation of rod-like nanocrystals.⁴ The electrostatic interactions not only shift the isotropic-cholesteric phase transition to lower concentrations (typically in the order of a few weight percent) but also increase the cholesteric pitch as the ionic concentration of the aqueous phase decreases.⁵

Molecular cellulose is inherently chiral, and it is conjectured that this chirality is transferred from the molecular level to the macroscopic scale through an intermediate structure. Cellulose microfibrils, which constitute crystalline substructures of cellulosic fibers, exhibit a twist along their long axis.⁶ Molecular simulations have demonstrated that the length scale of this internal twist,

referred to as the microscopic pitch, depends on the width of the microfibril, with the degree of twisting being inversely proportional to the cross-sectional surface area of the fibril.⁷

The mechanism behind the transfer of chirality has been a subject of debate, but recent theoretical and experimental findings strongly suggest a correlation between the degree of twisting in the cholesteric phase, represented by the cholesteric pitch, and the presence of chiral bundles composed of cellulose microfibrils.^{8,9} Specifically, it has been demonstrated that the theoretical predictions of the cholesteric pitch, obtained using Onsager theory for chiral particles and modeling CNCs as chiral hard bundles of spherocylinders, aligned well with experimental measurements.⁸ Furthermore, it has been observed that the relationship between the microscopic pitch of the bundles, which determines the degree of twisting within a bundle, and the cholesteric pitch is non-monotonic. Additionally, the size and aspect ratio of the bundles were found to affect the cholesteric pitch, with a larger aspect ratio of the bundle resulting in a larger cholesteric pitch. Moreover, the presence of bidispersity in the system was found to increase the cholesteric pitch compared to a monodisperse system.

These findings suggest that fractionation of length polydisperse systems could offer a means to tailor the cholesteric pitch. To explore this possibility, we perform a comprehensive theoretical investigation of various factors that affect the cholesteric pitch of CNC suspensions.

More specifically, we examine how the length of the particles and the degree of twisting of the bundles influence the cholesteric pitch. Additionally, we investigate the effect of polydispersity and surface charge on cellulose microfibrils, offering valuable predictions that can assist in understanding the correlation between the microscopic characteristics of CNCs and system properties and how they relate to the resulting cholesteric pitch. Finally, we analyze how the cholesteric pitch varies with the fraction of chiral bundles present in CNC suspensions.

II. MODEL OF CNCs

To conduct a theoretical examination of the different factors influencing the cholesteric pitch in CNC suspensions, we employ the model introduced in Ref. 8 and represent CNCs as twisted bundles of microfibrils, as illustrated in Fig. 1. The microfibrils of a CNC bundle are modeled as $N_{sc} = 4$ achiral hard spherocylinders with a fixed diameter D and an end-to-end length L . Throughout the remainder of the paper, we use D as our unit of length. The chirality of the bundles arises from the microscopic pitch p , which is inherited from the individual microfibrils and results in a twist between adjacent microfibrils. We quantify the degree of twisting in the bundles by introducing a reduced internal wavevector, $q_{int} = 2\pi/p$. To be more specific, we choose the twist axis to be parallel to the z -axis in the particle frame of reference, with the center of the twist axis coinciding with the center of mass of the bundle.⁸ Points within the bundle, denoted by (x, y, z) , undergo a rotation by an angle $\alpha_{int} = 2\pi z/p$. The total width w of a chiral bundle can vary, either smaller or larger than $N_{sc}D$, allowing for some degree of overlap between the crystallites. Here, we consider the same spherocylinder overlap of the bundle as described in Ref. 8, which is defined as the total width of the bundle $w = CN_{sc}D$ with a constant factor $C = 0.75$. The interactions between the bundles are exclusively governed by excluded-volume

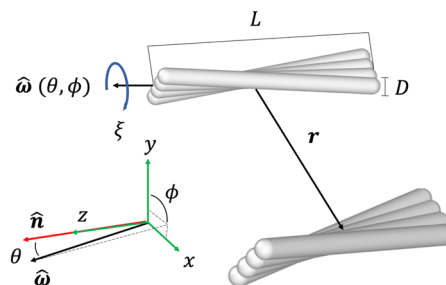


FIG. 1. Two CNC bundles, modeled as $N_{sc} = 4$ achiral hard spherocylinders of length L and diameter D , with a center-of-mass separation r . The orientations are given by the Euler angles θ , ϕ , and ξ , where the long-axis orientation $\hat{\omega}$ is defined by the former two (relative to the nematic director \hat{n}) and the internal angle ξ defines rotations around $\hat{\omega}$.

interactions. In Sec. IX, however, we further explore the effect of surface charge on the system. In this section, we also describe the interactions between the bundles, which include a screened-Coulomb interaction in addition to the hard-particle interaction.

III. DENSITY FUNCTIONAL THEORY FOR POLYDISPERSE SYSTEMS OF CNCs

We examine the effect of both the length and the length polydispersity of the CNC bundles on the equilibrium cholesteric pitch P of the cholesteric phase of CNCs using classical density functional theory (DFT) for chiral nematic phases.^{8,10–12} To achieve this, we consider a normalized length distribution $\mathcal{P}(l)$, where $l = L/L_0$ represents a renormalized length. Specifically, we consider a length polydisperse density distribution denoted by $c(l) = c_0 \mathcal{P}(l)$, where $c_0 = Nv_0/V$ represents a dimensionless number density. Here, N , V , and v_0 represent the number of particles in the system, the system volume, and the characteristic excluded volume of a particle, respectively. The value of v_0 is approximated as $v_0 = \pi L_0^2 D_B/4$ and represents the second virial coefficient of the chiral bundles in the isotropic phase under the condition $L_0 \gg D_B$, where D_B denotes a suitably selected width of the bundle. Our estimation is that $D_B = D\sqrt{CN_{sc}}$. This estimation is derived by mapping the bundle onto a cylindrical rod with a diameter D_B that has the same length L_0 and volume as the bundle. For additional information, please refer to the Appendix. It is important to note that if the particle consists of a single microfibril, meaning $D_B = D$, we recover the conventional dimensionless concentration for rods, which is expressed as $c_0 = \pi L_0^2 DN/(4V)$.

The Helmholtz free energy $F[\rho]$ of a polydisperse suspension of CNCs is a functional of $\rho(\mathbf{r}, \mathcal{R}, l)$, which represents the density distribution of particles at position \mathbf{r} in Cartesian space. Here, the density distribution depends on a reduced length l and a particle orientation defined by a 3×3 rotation matrix \mathcal{R} , characterized by the polar angle $\theta \in [0, \pi]$, azimuthal angle $\phi \in [0, 2\pi]$, and the internal azimuthal angle $\xi \in [0, 2\pi]$, representing the particle's rotation around its long axis. The density distribution satisfies the normalization condition, ensuring that the total number of particles in the system is defined as $N = \int d\mathbf{r} \int dl \int d\mathcal{R} \rho(\mathbf{r}, \mathcal{R}, l)$, where $d\mathcal{R} = d\xi d\phi d\cos\theta$.

Within Onsager's second virial approximation, the Helmholtz free energy per unit volume can be expressed as a sum of ideal and

excess contributions, $v_0\beta F[\rho]/V = f[\rho] = f_{\text{id}}[\rho] + f_{\text{ex}}^{(q)}[\rho]$, where $\beta = 1/k_B T$ represents the inverse temperature, T is the temperature, and k_B is the Boltzmann constant.

The ideal part of the free-energy density functional, denoted as f_{id} , for a length polydisperse system of CNCs comprises both translational and orientational contributions,

$$f_{\text{id}}[\rho] = \int dl c(l) (\ln [c(l) \gamma_0] - 1) + \int dl c(l) \int d\mathcal{R} \psi(\mathcal{R}, l) \times \ln [8\pi^2 \psi(\mathcal{R}, l)], \quad (1)$$

where $\psi(\mathcal{R}, l)$ represents a length-dependent orientation distribution function (ODF), and γ_0 is a dimensionless (and irrelevant) thermal volume.

The excess part of the Helmholtz free-energy functional, denoted as $f_{\text{ex}}^{(q)}$, depends on the macroscopic pitch P of the chiral nematic phase, which is related to the chiral wave vector $q = 2\pi/P$. If we define the chiral director (or helical axis) $\hat{\chi}$ to be aligned along the y -axis, the helical arrangement of the director field in the cholesteric phase implies that the ODF at any arbitrary position along the y -axis can be deduced from that at $y = 0$ by rotating it by an angle of $2\pi y/P = qy$ around the y -axis. Therefore, we find that the ODF defined at $\mathbf{r} = 0$, denoted as $\psi(\mathcal{R}, l)$, becomes $\psi(\mathcal{R}_{\hat{\chi}}(q\hat{\chi} \cdot \mathbf{r})\mathcal{R}, l)$ at \mathbf{r} , where $\mathcal{R}_{\hat{\chi}}(q\hat{\chi} \cdot \mathbf{r})$ represents a rotation around the chiral director $\hat{\chi}$ (which coincides with the y -axis) by an angle of $q\hat{\chi} \cdot \mathbf{r} = qy$. Within the Onsager second-virial approximation, the excess part of a length polydisperse chiral nematic phase is expressed as follows:

$$f_{\text{ex}}^{(q)}[\rho] = \int dl dl' c(l) c(l') E^{(l, l', q)}, \quad (2)$$

where $E^{(l, l', q)}$ represents the angular-averaged excluded volume for two bundles with renormalized lengths l and l' ,

$$E^{(l, l', q)} = -\frac{G(\eta)}{2v_0} \int d\mathbf{r} \int d\mathcal{R} d\mathcal{R}' \psi(\mathcal{R}_q, l) \psi(\mathcal{R}', l') \times f(\mathcal{R}_q, \mathcal{R}', l, l', \mathbf{r}), \quad (3)$$

with $\mathcal{R}_q = \mathcal{R}_{\hat{\chi}}(q\hat{\chi} \cdot \mathbf{r})\mathcal{R}$, and where the term $G(\eta) = (1 - 3\eta/4)/(1 - \eta)^2$ represents the Parsons–Lee correction factor. Here, η represents the volume fraction, which can be expressed as $\eta = v_B N/V$, where v_B corresponds to the volume of a bundle, which we calculate through Monte Carlo integrations.^{13,14} The Parsons–Lee factor approaches unity for rods that are infinitely long and slender.

Furthermore, we make the assumption that the local structure of the chiral nematic phase is locally uniaxial and remains unchanged under rotations around the main particle axis. The local uniaxiality assumption implies that any non-cylindrically symmetric characteristics of the particle are effectively averaged out. As a consequence, the ODF exhibits rotational symmetry around the local nematic director \hat{n} and the long axis of the particles. Hence, the ODF, denoted as $\psi(\mathcal{R}, l) = \psi(\theta, l)$, depends solely on the polar angle θ relative to \hat{n} .

A. Onsager theory

For a monodisperse system, the coefficients $E^{(l, l', q)}$ in Eq. (3) can be computed using Monte Carlo integration techniques, as demonstrated in Refs. 8, 10, and 11. Subsequently, the resulting

Helmholtz free energy $F[\rho]$ can be minimized with respect to $\psi(\theta, l)$ for a fixed density c_0 . This process is repeated for various values of the inverse pitch length q . Finally, the equilibrium pitch of the cholesteric phase is obtained by minimizing the free energy with respect to q . We will refer to this approach as the full Onsager theory.

B. Onsager–Straley theory

In Ref. 8, the Onsager theory approach was extended to a binary mixture of CNCs. This extension involves the computation of inter- and intra-species excluded volume terms and the minimization of the Helmholtz free energy with respect to the ODFs of each species as well as the chiral wavevector q . However, calculating the equilibrium pitch for a polydisperse system using the full Onsager theory approach is exceptionally computationally intensive.

We, therefore, resort to Straley's theory,¹⁵ which is applicable in the weak-chirality regime, and combine it with Onsager's theory. This approach is commonly referred to as the Onsager–Straley theory. Given that the cholesteric phase of CNCs is typically characterized by weak chirality, Straley's theory is expected to offer a suitable approach.

To achieve this, we expand the dimensionless free energy $f^{(q)}[\rho]$ to second order in q ,

$$f^{(q)}[\rho] = f^{(q=0)}[\rho] + \beta K_T q + \frac{1}{2} \beta K_2 q^2 + \mathcal{O}(q^3), \quad (4)$$

where we introduced the chiral strength

$$\beta K_T = \left. \frac{df_{\text{ex}}^{(q)}[\rho]}{dq} \right|_{q=0}, \quad (5)$$

and the twist elastic constant

$$\beta K_2 = \left. \frac{d^2 f_{\text{ex}}^{(q)}[\rho]}{dq^2} \right|_{q=0}. \quad (6)$$

In the case of polydisperse chiral phases of chiral nanorods, q can be computed directly from the length-averaged K_T and K_2 ,¹⁶

$$q_0 = -\frac{K_T}{K_2} = -\frac{\iint dl dl' c(l) c(l') K_T^{(l, l')}}{\iint dl dl' c(l) c(l') K_2^{(l, l')}}, \quad (7)$$

which is valid when the cholesteric pitch is much larger than the typical length of the particles, i.e., $P \gg L_0$. As previously mentioned, the equilibrium cholesteric pitch is then $P = 2\pi/q_0$. Here, the length-specific splay, twist, and bend elastic constants, $K_1^{(l, l')}$, $K_2^{(l, l')}$, and $K_3^{(l, l')}$, respectively, and the length-specific chiral strength, $K_T^{(l, l')}$, within the format of Onsager's second-virial theory read^{17,18}

$$\begin{aligned}\beta K_1^{(l,l')} &= \frac{G(\eta)}{2\nu_0} \int d\mathbf{r} \iint d\mathcal{R}d\mathcal{R}' \dot{\psi}(\theta, l) \dot{\psi}(\theta', l') \\ &\quad \times f(\mathcal{R}, \mathcal{R}', l, l', \mathbf{r}) y^2 \omega_y \omega'_y, \\ \beta K_2^{(l,l')} &= \frac{G(\eta)}{2\nu_0} \int d\mathbf{r} \iint d\mathcal{R}d\mathcal{R}' \dot{\psi}(\theta, l) \dot{\psi}(\theta', l') \\ &\quad \times f(\mathcal{R}, \mathcal{R}', l, l', \mathbf{r}) y^2 \omega_x \omega'_x, \\ \beta K_3^{(l,l')} &= \frac{G(\eta)}{2\nu_0} \int d\mathbf{r} \iint d\mathcal{R}d\mathcal{R}' \dot{\psi}(\theta, l) \dot{\psi}(\theta', l') \\ &\quad \times f(\mathcal{R}, \mathcal{R}', l, l', \mathbf{r}) z^2 \omega_y \omega'_y, \\ \beta K_T^{(l,l')} &= \frac{G(\eta)}{2\nu_0} \int d\mathbf{r} \iint d\mathcal{R}d\mathcal{R}' \dot{\psi}(\theta, l) \dot{\psi}(\theta', l') \\ &\quad \times f(\mathcal{R}, \mathcal{R}', l, l', \mathbf{r}) y \omega'_x,\end{aligned}\quad (8)$$

where $\hat{\chi}$ is taken to be parallel to the y -axis, $\dot{\psi}(l, \theta) = d\psi(l, \theta)/d \cos \theta$ is the derivative of the ODF, and ω_i is the i -component ($i = x, y, z$) of the orientation $\hat{\omega}$ of the long-axis of the particle. Note that we also included here the expressions for the length-specific splay and bend elastic constants, $K_1^{(l,l')}$ and $K_3^{(l,l')}$, respectively, for completeness.

The length-specific elastic constants $K_i^{(l,l')}$ with $i \in 1, 2, 3$ and chiral strength $K_T^{(l,l')}$ rely on a length-specific orientation distribution function $\psi(\theta, l)$. To obtain an expression for $\psi(\theta, l)$, we assume strong nematic ordering, allowing us to use the Gaussian ansatz for the trial ODF,^{16,19,20}

$$\psi(\theta, l) = \frac{1}{Z} \frac{\alpha(l)}{4\pi} \exp\left[-\frac{1}{2}\alpha(l)\theta^2\right], \quad (9)$$

where $\alpha(l)$, a length-dependent variational parameter, represents the width of the Gaussian distribution, and Z is a normalization constant. The argument θ is defined for $0 \leq \theta \leq \pi/2$. For $\pi/2 < \theta \leq \pi$, we apply the polar mirror argument ($\pi - \theta$) to maintain the apolarity of ψ . To derive an expression for $\alpha(l)$, we first consider the ideal part of the free-energy density by inserting Eq. (9) into Eq. (1). By taking the asymptotic limit of large $\alpha(l)$,²¹ we find

$$\begin{aligned}f_{\text{id}}[\rho] &= \int dlc(l) (\ln[c(l)\nu_0] - 1) + \left(\frac{2\pi}{Z}\right) \int dlc(l) \\ &\quad \times \left[\ln \alpha(l) + \ln\left(\frac{2\pi}{Z}\right) - 1\right].\end{aligned}\quad (10)$$

In the Onsager limit $L_0 \gg D$ and under the assumption of weak chirality, the excluded volume $E(l, l')$ can be approximated as

$$E^{(l,l')} = \frac{4G(\eta)l l'}{\pi} \int d\mathcal{R}d\mathcal{R}' |\sin(\gamma(\mathcal{R}, \mathcal{R}'))| \psi(\theta, l) \psi(\theta', l'), \quad (11)$$

where γ represents the angle between the long axis orientations of the particles, denoted as $\hat{\omega}$ and $\hat{\omega}'$, respectively (see $\hat{\omega}$ in Fig. 1). For θ, θ' , and γ , all of which are very small in the limit $\alpha(l) \gg 1$, we can employ the trigonometric relation $\cos \gamma = \cos \theta \cos \theta' + \sin \theta \sin \theta' \cos \phi$, with ϕ indicating the angle between the

projections of the bundles onto a plane perpendicular to the director. This relation yields $\gamma^2 \simeq \theta^2 + \theta'^2 - 2\theta\theta' \cos \phi$. By substituting this and Eq. (9) into Eq. (11), we obtain

$$\begin{aligned}E^{(l,l')} &= G(\eta) \frac{(2\pi)^2}{\pi} \frac{\alpha(l)}{Z} \frac{\alpha(l')}{Z} l l' \iint d\theta d\theta' (\theta^2 + \theta'^2) \\ &\quad \times \exp\left[-\frac{1}{2}\alpha(l)\theta^2 - \frac{1}{2}\alpha(l')\theta'^2\right].\end{aligned}\quad (12)$$

In this equation, two important steps have been taken. First, the azimuthal angle ϕ has been pre-averaged in the cosine term.²² Second, the internal angles, ξ and ξ' , have been integrated out. The remaining steps for the integration in Eq. (12) can be found in the Appendix to Ref. 22. This integration results in

$$\begin{aligned}E^{(l,l')} &= G(\eta) \left(\frac{2\pi}{Z}\right)^2 l l' \frac{4}{\sqrt{2\pi}} \frac{\sqrt{\alpha(l)} \sqrt{\alpha(l')}}{\sqrt{\alpha(l)} \sqrt{\alpha(l')}} \\ &= G(\eta) \left(\frac{2\pi}{Z}\right)^2 l l' \sqrt{\frac{8}{\pi} \left(\frac{1}{\alpha(l)} + \frac{1}{\alpha(l')}\right)}.\end{aligned}\quad (13)$$

Substituting Eqs. (10) and (13) into $f[\rho]$ and minimizing the free energy density with respect to the non-conserved orientational degrees of freedom yields^{16,20}

$$\begin{aligned}\frac{\delta f}{\delta \alpha(l)} &= \left(\frac{2\pi}{Z}\right) \frac{c(l)}{\alpha(l)} - G(\eta) \left(\frac{2\pi}{Z}\right)^2 \sqrt{\frac{8}{\pi} \frac{lc(l)}{2\alpha^2(l)}} \\ &\quad \times \int dl' l' c(l') \left(\frac{1}{\alpha(l)} + \frac{1}{\alpha(l')}\right)^{-1/2}.\end{aligned}\quad (14)$$

Applying the stationary condition, $\delta f / \delta \alpha(l) = 0$,²⁰ yields the following self-consistency equation:

$$\alpha(l) = \frac{4(G(\eta)c_0)^2}{\pi} \left(\frac{2\pi}{Z}\right)^2 2l^2 \left\{ \int dl' l' \mathcal{A}(l') \left[1 + \frac{\alpha(l)}{\alpha(l')}\right]^{-1/2} \right\}^2. \quad (15)$$

Throughout the derivation, we have retained the normalization constant Z explicitly and generalized our analysis beyond infinitely long and slender rods by introducing $G(\eta)$. Notably, the Parsons–Lee factor $G(\eta) \geq 1$ in Eq. (15) favors a more sharply peaked ODF as it appears squared in the prefactor. Moreover, as the concentration increases and $\alpha(l)$ becomes larger, the factor $2\pi/Z$ tends toward unity. Consequently, at the high concentration limit, this factor can be neglected. For the monodisperse case ($l = l' = 1$) and at high particle concentrations where $2\pi/Z \simeq 1$, we obtain $\alpha_0 = 4(G(\eta)c_0)^2/\pi$. This result represents a Parsons–Lee-corrected expression for α , as presented in Ref. 19. By combining Eq. (9) with Eq. (15) in Eq. (8), we can calculate the equilibrium chiral wavevector q_0 as defined in Eq. (7) within the Onsager–Straley approach for any length polydisperse concentration distribution $c(l)$.

To summarize, the Onsager–Straley theory is based on an expansion of the full free energy functional for small q , with coefficients evaluated in the achiral limit ($q = 0$). These coefficients, namely the chiral strength and the twist elastic constant, enable a direct estimation of the cholesteric pitch. We also note that the Onsager–Straley theory is only valid in the limit of weak chirality

due to the small- q expansion. In Sec. IV, we investigate the applicability of the weak chirality limit, as assumed by Onsager–Straley’s theory, to the cholesteric phases of twisted bundles of cellulose microfibrils. To accomplish this, we compare the predictions derived from Onsager–Straley’s theory with the full solutions obtained from Onsager’s theory, not limited to Straley’s weak chirality regime.

IV. VALIDITY OF THE ONSAGER-STRALEY THEORY FOR SUSPENSIONS OF CNCs

To assess the applicability of the weak chirality limit of the Onsager–Straley theory to cholesteric phases of twisted bundles of cellulose microfibrils, we compare the predictions of the Onsager–Straley theory with the full solution from the Onsager theory across a range of relevant CNC packing fractions. In Fig. 2, we plot the predictions for the cholesteric pitch P of a monodisperse system of CNC bundles with an aspect ratio $L_0 = 14D$, bundle width $w = 3.1D$, and microscopic pitch $p = 54D$, corresponding to a length $L_0 = 130.2$ nm and microscopic pitch $p = 500$ nm for microfibrils with a diameter $D = 9.3$ nm, as a function of CNC packing fraction η as obtained from the Onsager–Straley theory [Eq. (7)] using the Gaussian ansatz for the ODF. For comparison, we also plot the full solutions from Onsager theory. We find that the Onsager–Straley predictions agree rather well with the full Onsager solution. The predictions slightly overestimate the pitch P at low packing fractions; however, the difference decreases with increasing packing fractions. This is to be expected as the ODF becomes more strongly peaked around the (local) nematic director as the packing fraction increases. Consequently, the Gaussian Ansatz becomes an increasingly good approximation for the self-consistent ODF derived from the full Onsager solution. This can also be appreciated by comparing the nematic order parameters S as predicted by the full Onsager theory with those obtained from the Gaussian ansatz $\alpha_0 = 4(G(\eta)c_0)^2/\pi$ for a monodisperse system, where the nematic order parameter is defined by $S = \int d\mathcal{R} \mathcal{P}_2(\theta) \psi(\theta)$ with $\mathcal{P}_2(\theta) = (3/2)\cos^2\theta - 1/2$ the second Legendre polynomial. The inset in Fig. 2 demonstrates that the nematic order parameter S as obtained from the full Onsager theory approaches the one obtained from the Gaussian ansatz upon

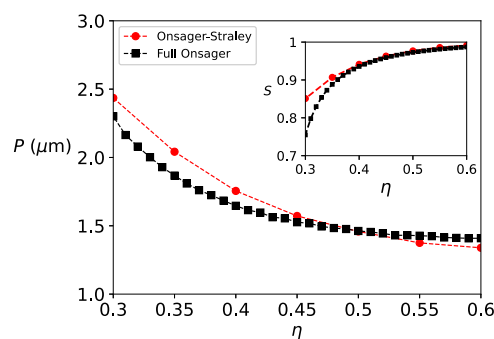


FIG. 2. The cholesteric pitch P in μm of a suspension of monodisperse CNC bundles with an aspect ratio $L_0 = 14D$, microscopic pitch $p = 54D$, width $w = 3.1D$, and $D = 9.3$ nm as a function of the CNC packing fraction η as obtained using Onsager–Straley theory. For comparison, we also plot the full solutions from Onsager theory. The inset shows the corresponding nematic order parameter S as a function of η .

increasing the packing fraction. However, the nematic order parameter S is slightly higher using the Gaussian approximation as the ODFs are slightly more peaked due to the Parsons–Lee correction in Eq. (15).

In summary, our predictions for the macroscopic pitch P of cholesteric phases in twisted bundles of cellulose nanocrystals, using the Onsager–Straley theory, show good agreement with the full Onsager predictions. Given the previous findings in Ref. 8, where the full Onsager predictions aligned well with experimentally determined pitches in apolar solvents,^{9,23} it is reasonable to expect that the Onsager–Straley predictions would similarly correspond favorably with these experimental values.

In the remainder of the paper, we will employ the Onsager–Straley approach to investigate the effect of particle shape, length polydispersity, surface charge, and fraction of twisted bundles on the cholesteric pitch P .

V. THE EFFECT OF LENGTH AND CHIRALITY OF CNC BUNDLES

We first calculate the cholesteric pitch P for a suspension of CNC bundles with two different end-to-end lengths L_0 and two different microscopic pitches p using the Onsager–Straley approach. In Fig. 3, we plot the cholesteric pitch P as a function of packing fraction η for CNCs with a length $L_0 = 14D$ and $L_0 = 21D$ and a microscopic pitch $p = 54D$ (a) and $p = 500D$ (b). For CNCs with strong chirality, as characterized by a small microscopic pitch p shown in Fig. 3(a), we observe a significant dependence of the cholesteric pitch P on the length L_0 of the CNC bundles. More specifically, for a CNC

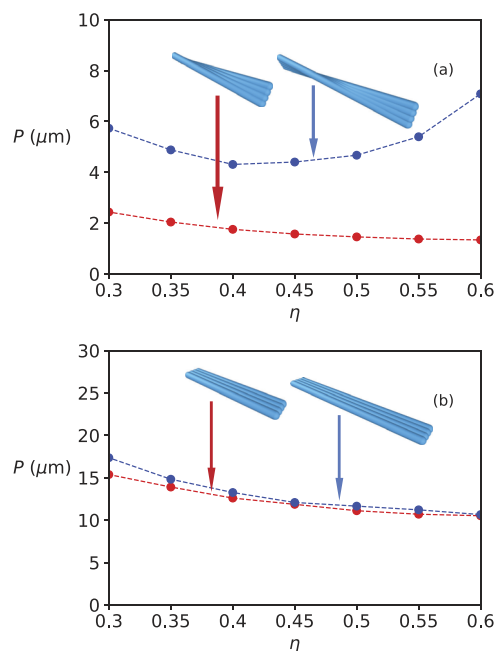


FIG. 3. The cholesteric pitch P in μm as a function of the CNC volume fraction η of a cholesteric phase of monodisperse CNC bundles with an aspect ratio $L_0 = 14D$ (red) and $L_0 = 21D$ (blue) and microscopic pitch $p = 54D$ (a) and $p = 500D$ (b), all with a width $w = 3.1D$ and $D = 9.3$ nm.

system with a length-to-diameter ratio of $L_0 = 14D$, we observe a monotonic decrease in the macroscopic pitch P as the packing fraction η increases. This behavior indicates that as the CNC bundles become more densely packed, the cholesteric pitch decreases consistently. However, for CNCs with a larger length-to-diameter ratio of $L_0 = 21D$ and a short microscopic pitch $p = 54D$, we observe a non-monotonic relationship between the macroscopic pitch P and the packing fraction η . In the case of weakly chiral CNCs, as shown in Fig. 3(b), changes in the particle length have little impact on the resulting macroscopic pitch P .

It is intriguing to draw a comparison between our key observations regarding CNC bundles and another particle system, specifically hard helices, as investigated in Ref. 11. Our primary findings indicate that, in the case of CNC bundles, an increase in particle length results in a longer cholesteric pitch P , corresponding to a weaker cholesteric character. This observation is consistent with Ref. 8. Additionally, for strongly twisted bundles (i.e., small p),

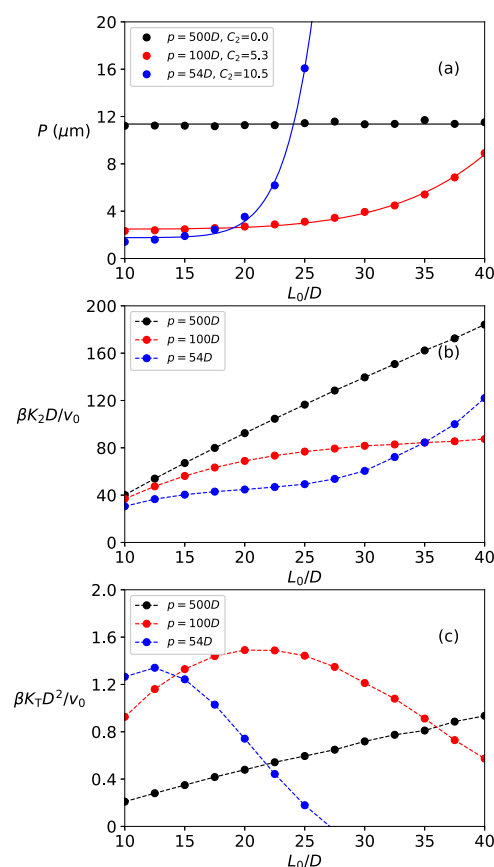


FIG. 4. (a) The cholesteric pitch P in μm , (b) the twist elastic constant $K_2^{(l,l')}$, and (c) the chiral strength $K_T^{(l,l')}$, with $l = l' = 1$ as defined in Eq. (8), of a cholesteric phase of monodisperse CNC bundles for varying microscopic pitches ($p = 54D$, $100D$, and $500D$), a width $w = 3.1D$, $D = 9.3$ nm, and a volume fraction $\eta = 0.4$, all as a function of the aspect ratio L_0/D . The solid lines in (a) represent fits to the data, following the form $P_{\text{fitting}} = C_1 (L_0/D)^{C_2} + C_3$.

the relationship between P and packing fraction η becomes non-monotonic for sufficiently long CNC bundles, while weakly chiral bundles exhibit a monotonic dependence of P on η . Remarkably, both of these observations align with the behaviors observed for hard helices, as studied in Ref. 11.

To examine in more detail the effect of bundle length on the cholesteric pitch P , we plot in Fig. 4(a) the particle-length dependency of P at volume fraction $\eta = 0.4$ for three microscopic pitches, $p = 54D$, $p = 100D$, and $p = 500D$. The behavior of the cholesteric pitch P as a function of particle length L_0/D depends strongly on the microscopic pitch p , as already hinted at in Fig. 3. In the case of strongly twisted bundles with microscopic pitches of $p = 54D$ and $p = 100D$, the cholesteric pitch P shows a significant and rapid increase as the particle length L_0 increases. However, for weakly twisted bundles with a microscopic pitch of $p = 500D$, the increase in cholesteric pitch within the range of particle lengths L_0/D considered is practically negligible. Within this experimentally relevant range of particle lengths L_0 for CNCs, the dependency on length becomes less significant for sufficiently low degrees of twisting. However, the cholesteric pitch P varies considerably for different values of p . For example, at $L_0 = 15D$, the pitches for $p = 54D$ and $p = 100D$ are quite similar, whereas the pitch for $p = 500D$ is several times larger.

To delve deeper into the markedly different behaviors observed for the three different microscopic pitch lengths p , we consider their influence on K_T and K_2 , which are predictive of the cholesteric pitch P [see Eq. (7)]. The twist elastic constant K_2 increases with L_0/D for all three values of p , even though the length-dependence behavior is very different [Fig. 4(b)]. However, the behavior of the chiral strength K_T is more intricate, as depicted in Fig. 4(c). This aspect is crucial in understanding the substantial increase in P with increasing L_0/D for short microscopic pitches p . For sufficiently long p , the chiral strength monotonically increases with L_0/D . In contrast, for the two shorter p values, the behavior is non-monotonic, and it decreases for relatively large L_0/D . Remarkably, the chiral strength even changes sign as q_0 changes sign, resulting in a reversal of the cholesteric handedness. We will further elaborate on these effects related to the degree of chiral twist in the bundle in Fig. 6.

VI. THE EFFECT OF LENGTH POLYDISPERSITY OF CNC BUNDLES

Next, we investigate the effect of length polydispersity of CNC bundles on the cholesteric pitch P . Our Monte Carlo (MC) integration procedure follows the same approach as described in Ref. 8, where we sample random orientations of pairs of CNC bundles. However, we made some adjustments to the sampling procedure. The lengths of the CNC bundles are sampled from the specified length distribution. To determine $\alpha(l)$ for a given length distribution $\mathcal{P}(l)$, we solve Eq. (15) self-consistently. By discretizing the length distribution, we obtain a corresponding distribution of $\alpha(l)$. This distribution can be pre-calculated and incorporated into the MC integration process. Additionally, we assume the center-of-mass of the first CNC bundle to be positioned at the origin. The spatial coordinate of the second CNC bundle is randomly sampled within the largest sphere, where two particles of lengths l and l' could potentially overlap. This modified sampling approach allows us to perform the MC integration process and to compute the excluded volume

[Eq. (3)] and elastic constants [Eq. (8)]. As in Ref. 8, the overlap of two CNC bundles was evaluated by checking overlaps between the respective N_{sc} hard spherocylinders.

In Fig. 5, we demonstrate the impact of length polydispersity σ on the cholesteric pitch P , including its two contributions, K_2 and K_T [see Eqs. (7) and (8)]. The polydispersity σ is defined as

$$\sigma = \left(\frac{\langle l^2 \rangle - \langle l \rangle^2}{\langle l \rangle^2} \right)^{1/2}. \quad (16)$$

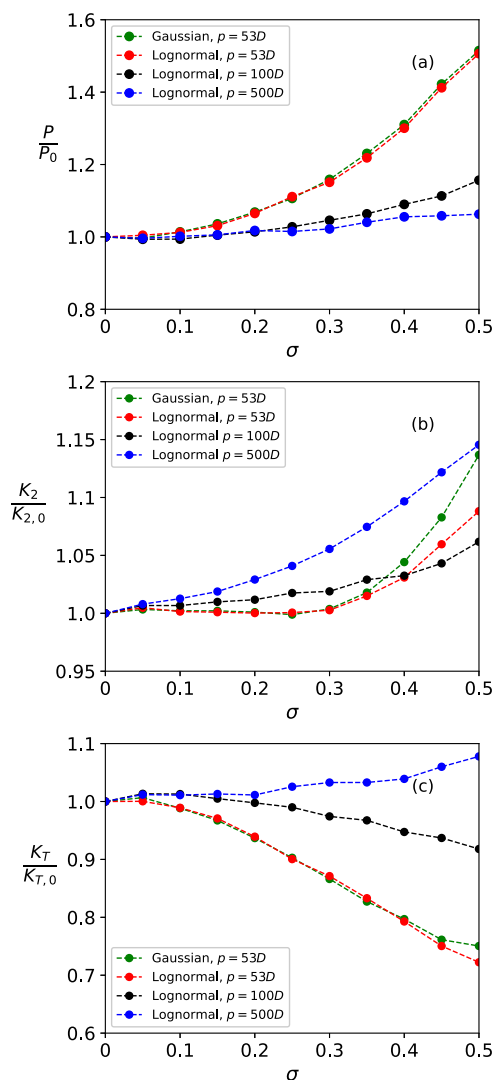


FIG. 5. (a) The cholesteric pitch P , (b) the twist elastic constant K_2 , and (c) the chiral strength K_T as a function of polydispersity σ of a lognormal and Gaussian length distribution of a cholesteric phase of CNC bundles with an aspect ratio $L_0 = 14D$ and microscopic pitch $p = 53D$, $p = 100D$, and $p = 500D$, respectively, at a packing fraction $\eta = 0.37$, corresponding to a nematic order parameter $S = 0.93$ (for $\sigma = 0$). Here, P_0 , $K_{2,0}$, and $K_{T,0}$ represent the cholesteric pitch, twist elastic constant, and chiral strength in the monodisperse case ($\sigma = 0$).

In general, the cholesteric pitch P as well as K_2 increase with polydispersity σ . However, the shape of the curves for K_2 varies depending on the degree of twisting of the bundle. In the case of weakly twisted bundles ($p = 100D$ and $500D$), K_2 increases gradually with polydispersity σ , whereas for strongly twisted particles ($p = 53D$), K_2 remains unaffected by polydispersity until σ reaches 0.3, beyond which it rapidly increases. The relationship for K_T is more complex, transitioning from a decrease with σ for strongly twisted particles to an increase with σ for weakly twisted particles.

The results presented consider a lognormal length distribution that takes into account the explicit length dependency of the α -parameter, denoted as $\alpha(l)$. In all cases, the first moment is conserved, meaning that $\int dl l \mathcal{P}(l) = 1$.

Additionally, we provide results for a Gaussian length distribution at $p = 53D$, which exhibits a cholesteric pitch P that is virtually indistinguishable from the corresponding case with a lognormal length distribution. Consequently, we reach the same conclusion as in Ref. 16 on polydisperse slender rods with a soft chiral interaction. Namely, the specific shape of the length distribution becomes less significant compared to the degree of polydispersity, where an increase in the width of the length distribution results in a significant “stiffening” of the nematic phase with respect to a twist distortion.

VII. THE EFFECT OF MICROSCOPIC PITCH AND LENGTH POLYDISPERSITY

We now investigate in further detail the combined effect of microscopic pitch p and the length polydispersity of the CNC bundles on the cholesteric pitch P . In Fig. 6, we plot the equilibrium cholesteric wave number $q_0 L_0 = 2\pi L_0 / P$ as a function of the internal wave number $q_{int} L_0 = 2\pi L_0 / p$ of the CNC bundle for monodisperse ($\sigma = 0$) and polydisperse ($\sigma = 0.2$ and $\sigma = 0.4$) CNC suspensions

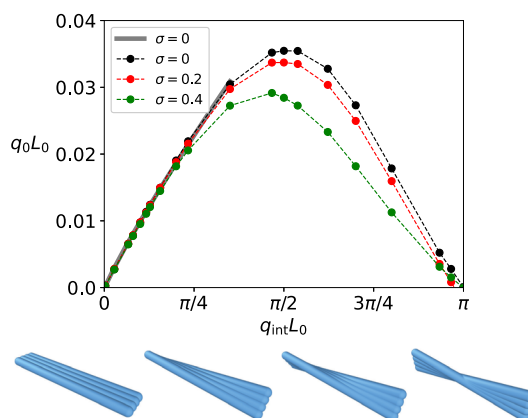


FIG. 6. The cholesteric wave number $q_0 L_0$ as a function of the internal wave number $q_{int} L_0$ for monodisperse ($\sigma = 0$) and polydisperse ($\sigma = 0.2$ and $\sigma = 0.4$) systems with lognormal length distributions of CNC bundles of length $L_0 = 14D$ and width $w = 3.1D$, $D = 9.3$ nm, and at a volume fraction $\eta = 0.31$. The gray fitted curve for $\sigma = 0$ is given by $C_1 (q_{int})^2 + C_3$, with $C_1 = 0.029$, $C_2 = 0.89$, and $C_3 = -0.00026$. Schematics of CNC bundles with an internal wave number of $q_{int} L_0 = 0.2, 1.5, 2.0, 2.9$ from left to right.

with an averaged bundle length $L_0 = 14D$, width $w = 3.1D$, diameter $D = 9.3$ nm, volume fraction $\eta = 0.31$, and a lognormal length distribution.

In the limit $q_{\text{int}} \rightarrow 0$, the twist within the bundle vanishes, resulting in an infinite cholesteric pitch ($q_0 \rightarrow 0$), corresponding to a uniaxial nematic phase. As the twisting of the bundle increases (starting from no twisting), there is a corresponding increase in the value of q_0 (or decrease in P) until a maximum value of q_0 is reached at an optimal degree of internal twist of the bundle ($q_{\text{int}} L_0 \approx \pi/2$). Beyond this optimum, as the bundle becomes increasingly twisted, q_0 starts to decrease again. In the case of an over-twisted bundle where $q_{\text{int}} L_0 \rightarrow \pi$, P tends toward infinity, indicating that the particles lose their chiral property. It is important to note that for $q_{\text{int}} L_0 > \pi$, the handedness of the particles changes, leading to a sign change in q_0 as a consequence. At first glance, the curve may appear to be symmetric about $q_{\text{int}} L_0 \approx \pi/2$ for the monodisperse case ($\sigma = 0$). However, upon closer examination, the curve exhibits a slight rightward skewness.

Furthermore, as polydispersity increases (cf. $\sigma = 0.2$ and 0.4), the effect becomes increasingly asymmetric about the optimum degree of bundle twist. Initially, at vanishing bundle twist, the effect of polydispersity is negligible. However, as the twist of the bundle increases, the importance of polydispersity gradually grows. For strongly twisted bundles, beyond the optimum twist, the relative difference between the monodisperse and polydisperse pitches remains significant.

The asymmetry around the maximum can be explained by Fig. 4. For small values of p (specifically $p = 54D$ and $100D$), there is a significant rise in the cholesteric pitch with particle length, unlike the cases with larger p values (such as $p = 500D$). In the regime of small p , the contribution of longer particles from the polydisperse length distribution becomes more prominent due to the strong dependence of pitch on particle length. Consequently, larger variations in q_0 are observed for different polydispersities, particularly in the range of larger $q_{\text{int}} L_0$, as depicted in Fig. 6, where the bundles exhibit strong twisting.

VIII. ELASTIC CONSTANTS

We now turn our attention to the elastic constants. Figure 7 presents the elastic constants for monodisperse and polydisperse ($\sigma = 0.3$) CNC bundles, along with reference values for rods consisting of a single microfibril. All the structures have an average aspect ratio of $L_0 = 14D$. The elastic constants are plotted as a function of the uniaxial order parameter S , allowing for a comparison of the two systems (bundles vs rods). This approach avoids comparing them based on the number density N/V and packing fraction η , as it is not possible for both of these parameters to be equal for the two systems simultaneously due to the presence of four microfibrils in each bundle. Notably, we found that the elastic constants are consistently higher for the bundles compared to the reference rods. However, the discrepancy between the bundles and rods is notably more pronounced for K_1 and K_2 compared to K_3 . More surprisingly, a polydispersity level as high as $\sigma = 0.3$ in bundle length has a minimal, almost negligible, effect on K_1 and K_2 , resulting in only a slight increase in K_3 compared to the monodisperse reference.

To further evaluate the elastic constants for rods at $S \approx 0.8$, we employ the Gaussian Ansatz (GA) for the ODF and compare the

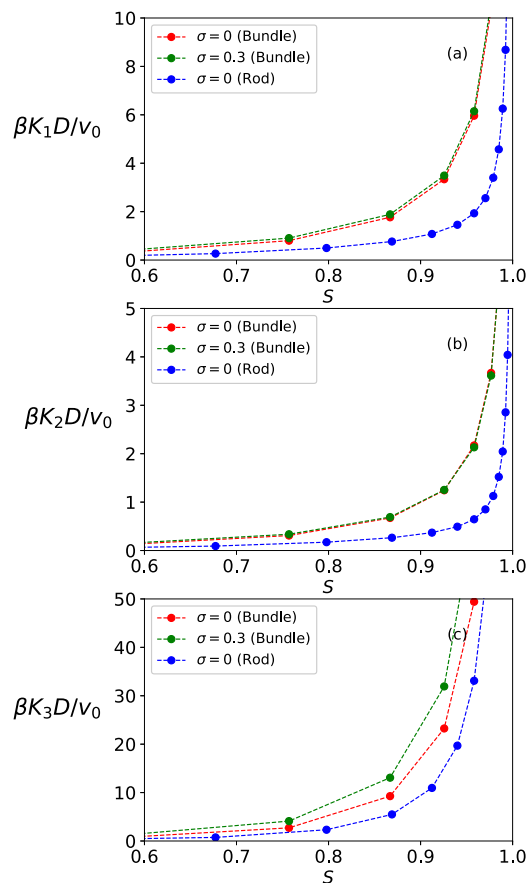


FIG. 7. Elastic constants (a) $\beta K_1 D/v_0$ (splay), (b) $\beta K_2 D/v_0$ (twist), and (c) $\beta K_3 D/v_0$ (bend) as a function of the nematic order parameter S for monodisperse ($\sigma = 0$) and polydisperse ($\sigma = 0.3$) systems with a lognormal length distribution of CNC bundles of length $L_0/D = 14$ along with the elastic constants for rods consisting of single microfibrils as a reference.

results with the corresponding predictions made by Straley (S),²⁴ where he utilized an approximate form of the Onsager's trial ODF, i.e., $\psi(\theta) = 1.483 \exp(-6.92 + 4.58 \cos^2 \theta + 2.0 \cos^4 \theta - 2.01 \cos^6 \theta + 2.28 \cos^8 \theta)$. The comparison reads: (GA/ S): $K_1 = 0.062/0.062$, $K_2 = 0.021/0.021$, and $K_3 = 0.30/0.39$. We thus find that the difference in the elastic constants as obtained by using the Gaussian Ansatz or Onsager's trial ODF is negligible to small.

Experimentally, the twist elastic constant for coated CNC was determined to be in the range of $K_2 \approx 0.02$ – 0.07 pN for weight fractions approximately ranging from 20 to 35 wt. %.²³ This system closely resembles the one in Ref. 8, albeit with toluene as the solvent. By employing the volumetric packing fraction-to-weight fraction conversion method outlined in Ref. 8, we can estimate K_2 to be in the range of 0.04 – 0.14 pN for weight fractions spanning from 27 to 35 wt. %. This corresponds to packing fraction values in the range $\eta = 0.19$ – 0.25 and nematic order parameter values in the range $S = 0.55$ – 0.76 . This comparison demonstrates that our predictions align with the experimental estimates, falling within the same range.

IX. CHARGED BUNDLES

We now shift our focus to CNC bundles in aqueous solutions, where electrostatic interactions play a significant role. As previously described, these interactions arise from the ionization of sulfuric groups on the surface of CNCs. The range of electrostatic interactions is influenced by the concentration of mobile ions present in the solvent. This includes the presence of dissociated counterions that interact with the ionized sulfuric groups on the CNC surface as well as any additional salt in the solution.

To model the interactions resulting from charges along the backbone of each microfibril within a CNC bundle, we employ a Yukawa-site model. This model discretizes the line charge uniformly. The total interaction energy between a pair of bundles is obtained by summing the pairwise Yukawa-site interactions between each individual bundle while excluding self-interactions. When two bundles do not overlap, the site-to-site energy can be expressed as follows:

$$\beta u(r) = \frac{l_B}{D} \frac{(Z/M)^2}{(1 + \kappa D/2)^2} \frac{\exp[-\kappa(r - D)]}{r/D}, \quad (17)$$

where Z denotes the charge on a spherocylinder, l_B is the Bjerrum length, $1/\kappa$ is the Debye screening length, M is the number of Yukawa sites representing the line charge, and r is the site-to-site distance. If the bundles overlap, the interaction potential becomes infinity, $\beta u(r) = \infty$, which is analogous to the hard-core interactions of uncharged CNC bundles. The electrostatic surface potential ϕ_0 of the spherocylinders (hence the bundles) is assumed to be uniform and is given by

$$\beta e \phi_0 = \frac{l_B}{D/2} \frac{(Z/M)}{(1 + \kappa D/2)}. \quad (18)$$

Figure 8 shows the effect of electrostatic screening on the cholesteric pitch P of charged CNCs with a surface potential of $\beta e \phi_0 = 2$ and 3, corresponding to 50 and 75 mV at 298 K, respectively. The linear charge is discretized with $M = 10$ sites, and the range of the Coulomb interactions is truncated at a site-to-site distance of $r = 20/\kappa$. The microfibril aspect ratio is $L_0 = 14D$, and the microscopic pitch is $p = 54D$ with $D = 9.3$ nm. Figure 8 reveals that an increase in screening, characterized by an increase in κD_{eff} , leads to a decrease in the cholesteric pitch, i.e., a shorter pitch length P . These findings align with experimental observations.^{5,25} Similar results were observed for hard helices exhibiting a short-ranged repulsive interaction. In these cases, the cholesteric pitch increased upon increasing the range of the soft interaction.¹¹ In addition, we find that the cholesteric pitch P decreases upon increasing the nematic order parameter S , as was also observed for uncharged bundles.

It is important to note that we use the Gaussian ansatz for the orientation distribution function in our Onsager–Straley approach. The width of the Gaussian distribution function is determined by a dimensionless number density $c_0 = \pi L_0^2 D_B N / 4V$ with $D_B = D\sqrt{CN_{sc}}$ [see Eq. (15)]. By assuming that the particles are characterized by an effective length L_0 and an effective diameter D that takes into account the electrostatic contributions, we can also compute an effective packing fraction η_{eff} for a given c_0 without explicitly

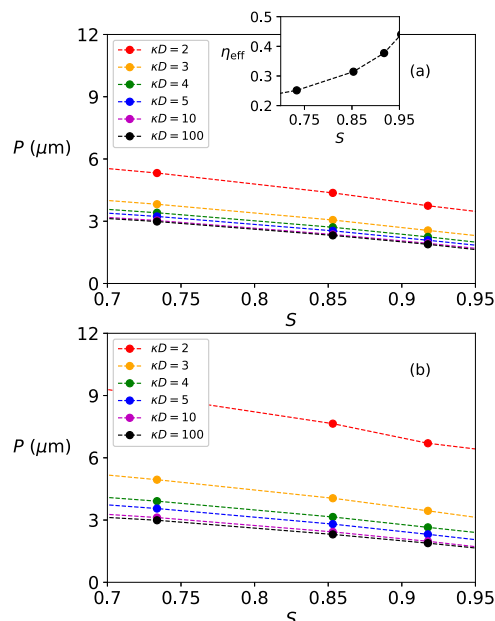


FIG. 8. The cholesteric pitch P as a function of the nematic order parameter S at varying electrostatic screening lengths κD for monodisperse bundles consisting of charged microfibrils with an aspect ratio $L_0 = 14D$, width $w = 3.1D$, $D = 9.3$ nm, and surface potential (a) $\beta e \phi_0 = 2$ and (b) $\beta e \phi_0 = 3$. The inset in (a) shows the effective packing fraction η_{eff} for a given S .

separating the hard-core contribution from the electrostatic contribution. Moreover, the width of the Gaussian distribution function determines the nematic order parameter S . In the inset, we show the relation between the nematic order parameter S and an effective packing fraction η_{eff} , which can be used to estimate the dependence of cholesteric pitch on the effective packing fraction.

When the screening length becomes on the order of the microfibril width D , the cholesteric pitch P becomes highly sensitive to changes in the ion concentration (or in κD) while keeping the nematic order parameter S constant. However, as the screening becomes stronger and the Debye screening length becomes significantly shorter than D , for example, when $\kappa D > 4$, the pitch becomes less sensitive to a further increase in salt concentration. Conversely, an increase in charge density (corresponding to a higher surface potential ϕ_0) at a constant nematic order parameter S leads to a notable increase in the pitch, particularly within the screening range of $\kappa D < 10$.

X. BINARY MIXTURES OF BUNDLES AND RODS

Real systems of CNCs exhibit significant polydispersity in terms of particle size. In addition, the size distribution within a suspension can be influenced by tip sonication.⁹ The CNC population can be broadly classified into several distinct “subspecies” that have varying impacts on the cholesteric pitch. These subspecies include aggregates, bundles, crystallites (individual microfibrils), and distorted particles resulting from sonication. The relative proportions of these classes depend on the degree of sonication, which typically breaks

down aggregates and bundles into their constituent units, namely microfibrils.

According to the first approximation, the system predominantly consists of two components: bundles and free crystallites. Hence, we can model these systems as binary mixtures composed of two distinct species: Bundles (B) act as chiral dopants, while rods (R) are inherently incapable of transferring chirality to the macroscopic scale. To describe the system, we extend the free-energy functional in Eqs. (1) and (2) for a binary mixture,

$$f^{(q)}[\rho] = \int dl c(l) \left(\ln [c(l) \nu_0] - 1 + \sum_i x_i \ln x_i \right) + \int dl c(l) \sum_i x_i \int d\mathcal{R} \psi_i(\mathcal{R}, l) \ln [8\pi^2 \psi_i(\mathcal{R}, l)] + \int dldl' c(l) c(l') \sum_i \sum_j x_i x_j E_{i,j}^{(l,l',q)}, \quad (19)$$

where $\psi_i(\mathcal{R}, l)$ denotes the length-dependent orientation distribution function of species $i = R, B$, x_B corresponds to the fraction of bundles in the system, given by $x_B = N_B / (N_B + N_R)$, and N_B and N_R denote the number of bundles and rods, respectively. The species-specific excluded volumes for bundle–bundle, rod–bundle, and rod–rod interactions are denoted by $E_{i,j}^{(l,l',q)}$, where i and j can represent either R (rods) or B (bundles).

Using Onsager–Straley’s theory, we predict the cholesteric pitch P for a binary mixture of rods and bundles. We employ the same ODF for both rods and bundles, denoted as $\psi_B = \psi_R = \psi$, and adopt the Gaussian ansatz for the ODF. This approach leads us to the same expression for the width of the Gaussian distribution, $\alpha(l)$, as in Eq. (15). We note that the length-dependent Gaussian width $\alpha(l)$ includes a Parsons–Lee correction that depends on a dimensionless number density $c_0 = N v_{\text{mix}} / V$, where v_{mix} denotes the second virial coefficient of the particles in the isotropic phase of the mixture and $N = N_B + N_R$. We approximate v_{mix} by a number fraction averaged excluded volume $v_{\text{mix}} = x_B^2 v_{BB} + 2x_B(1 - x_B) v_{RB} + (1 - x_B)^2 v_{RR}$ with $v_{BB} = \pi L_0^2 D_B / 4$, $v_{RR} = \pi L_0^2 D / 4$, and $v_{RB} = \pi L_0^2 (D_B + D) / 8$.

We compute the equilibrium chiral wave number q_0 of the cholesteric phase directly from the length-averaged and species-averaged K_T and K_2 ,

$$q_0 = - \frac{\iint dldl' c(l) c(l') \sum_i \sum_j x_i x_j K_{T,i,j}^{(l,l')}}{\iint dldl' c(l) c(l') \sum_i \sum_j x_i x_j K_{2,i,j}^{(l,l')}}. \quad (20)$$

We use a similar numerical MC integration scheme to evaluate these integrals as for the pure bundle systems above, but with the following adjustment: for each two-particle configuration, during the MC integration process, we randomly select either a rod or a bundle for each particle with a probability determined by their respective number fractions x_i .

We examine the impact of increasing the volume fraction of bundles, acting as chiral dopants, on the equilibrium chiral wave number q_0 for both monodisperse particles and length-polydisperse rods and bundles following a lognormal distribution with $\sigma = 0.4$. The results are depicted in Fig. 9. The bundle volume fraction, denoted as ζ_B , is calculated using the expression $\zeta_B = x_B v_B / (x_B v_B + (1 - x_B) v_R)$, where v_B and v_R are the volumes of a bundle and a rod, respectively.

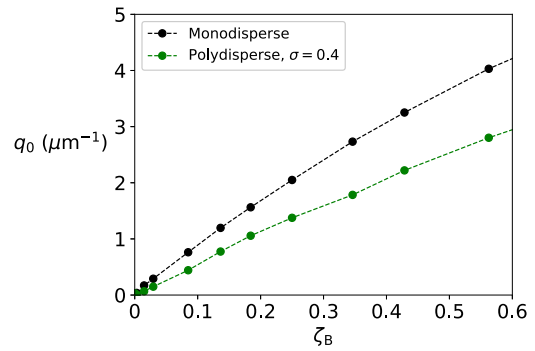


FIG. 9. The equilibrium cholesteric wavenumber q_0 as a function of the volumetric chiral dopant fraction ζ_B for a monodisperse and length-polydisperse (lognormal, $\sigma = 0.4$) binary mixture of bundles (the dopant) and rods, both with averaged length $L_0 = 14D$ and width $w = 3.1D$, $D = 6.5$ nm. The CNC packing fraction is $\eta = 0.4$, and the microscopic pitch is $p = 54D$.

As expected, when no bundles are present, the chiral wave number q_0 is found to be zero. However, as the fraction of bundles increases, q_0 also increases, leading to a larger degree of helical twisting. The observed behavior is rather similar to the experimental observations in Ref. 9, particularly when polydispersity is considered in the model, exhibiting a nearly linear relationship between q_0 and ζ_B . It is important to note that the experimental system in Ref. 9 is aqueous, where electrostatic interactions likely play a significant role. In our predictions, we have solely accounted for hard-particle interactions. However, as depicted in Fig. 8, the masking of the particle chirality due to electrostatics tends to primarily increase or decrease the cholesteric pitch, depending on the level of screening. This effect should not fundamentally change qualitative behavior. Our findings on binary mixtures of bundles and crystallites further support the hypothesis proposed by Parton *et al.*⁹ that bundles act as chiral dopants in a crystallite-rich environment, thereby triggering the self-assembly of a cholesteric phase.

XI. CONCLUSIONS

Using the second-virial Onsager–Straley theory and modeling CNC microfibril bundles as hard chiral bundles of spherocylinders, we demonstrate that the weak chirality limit of Straley’s theory provides an accurate approximation for the predictions obtained from the full Onsager theory, especially at high packing fractions. In addition, we extend the Onsager–Straley theory to encompass length-polydisperse systems and screened Coulomb interactions, employing Yukawa potentials between discretized line charges on the spherocylinders. Furthermore, we consider binary mixtures of CNC bundles and individual crystallites (rods), creating a more realistic representation of CNC systems.

Our first observation reveals the substantial influence of the degree of internal chirality within the bundles, characterized by the microscopic pitch p , on the cholesteric pitch P . The cholesteric chiral wave number q_0 reaches its maximum when the normalized internal chiral wave number $q_{\text{int}} L_0$ is approximately equal to $\pi/2$. The normalized internal chiral wave number serves as a measure of the degree of twisting of the particle.

Furthermore, we find that the effect of particle aspect ratio (L_0/D) and polydispersity on the cholesteric pitch P is moderate to weak when the particles exhibit weak twisting ($q_{\text{int}}L_0 \lesssim \pi/2$) and diminishes for $q_{\text{int}}L_0 \ll \pi/2$. However, for strongly twisted bundles ($q_{\text{int}}L_0 \gtrsim \pi/2$), this effect becomes substantial. Generally, an increased aspect ratio and polydispersity tend to increase the cholesteric pitch. Furthermore, in our comparison between a Gaussian and lognormal length distribution, we observe that, while keeping the same length polydispersity σ , the shape of the length distribution does not significantly impact the cholesteric pitch.

In addition, we demonstrate that the presence of long-ranged screened-Coulomb interactions tends to mask the inherent chirality of the bundles, leading to a larger cholesteric pitch.

Finally, our study provides further support for the hypothesis that microfibril bundles act as chiral dopants in CNC suspensions that are predominantly composed of crystallites (free singular microfibrils), which are incapable of stabilizing a cholesteric phase on their own. These results are in accordance with experimental observations reported by Parton *et al.*⁹

ACKNOWLEDGMENTS

The authors acknowledge the financial support from the Royal Swedish Academy of Engineering Sciences (Hans Werthén Foundation) and ERC Advanced Grant No. ERC-2019-ADV-H2020 884902, SoftML. Bundle images were made using the OVITO open visualization tool.²⁶

AUTHOR DECLARATIONS

Conflict of Interest

The authors have no conflicts to disclose.

Author Contributions

Tor Sewring: Formal analysis (equal); Funding acquisition (supporting); Investigation (equal); Methodology (equal); Software (lead); Visualization (equal); Writing – original draft (lead); Writing – review & editing (supporting). **Marjolein Dijkstra:** Conceptualization (lead); Formal analysis (equal); Funding acquisition (lead); Investigation (equal); Methodology (equal); Project administration (lead); Resources (lead); Software (supporting); Supervision (lead); Visualization (equal); Writing – original draft (supporting); Writing – review & editing (lead).

DATA AVAILABILITY

The data that support the findings of this study are available from the corresponding author upon reasonable request.

APPENDIX: DETERMINATION OF THE PARSONS-LEE CORRECTION

As mentioned in the main text, we employ a Parsons–Lee corrected form of the length-dependent width $\alpha(l)$ for the Gaussian orientation distribution function. The Parsons–Lee correction includes a dimensionless concentration $c_0 = Nv_0/V$, where $v_0 = \pi L_0^2 D_B/4$ denotes the second virial coefficient of hard rods in

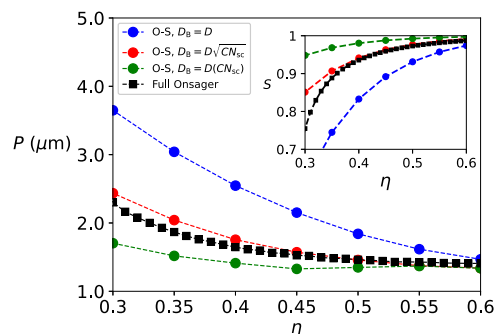


FIG. 10. The cholesteric pitch P in μm and the nematic order parameter S (inset) as a function of the packing fraction of the bundles of a suspension of monodisperse CNC bundles with an aspect ratio $L_0 = 14D$, microscopic pitch $p = 54D$, width $w = 3.1D$, and $D = 9.3$ nm as predicted by Onsager–Straley theory (O–S) using $D_B = D$ (blue), $D\sqrt{CN_{\text{sc}}}$ (red) and $D(CN_{\text{sc}})$ (green), respectively, with $C = 0.75$ correcting for overlapping spherocylinders. Full Onsager predictions (black) are obtained using Ref. 8.

the isotropic phase in the limit $L_0 \gg D_B$, and where D_B denotes a characteristic width. In the case of chiral bundles, we need to define the characteristic width of a bundle, D_B , which is bounded by the diameter of a single microfibril D and the width w of the bundle. Figure 10 shows that using $D_B = D$ overestimates the cholesteric pitch P , whereas $D_B = w \approx D(CN_{\text{sc}})$ underestimates P , where C is a correction factor accounting for the degree of overlap of the spherocylinders constituting the bundle. In addition, Fig. 10 demonstrates that the best agreement with the full Onsager predictions is obtained when $D_B = D\sqrt{(CN_{\text{sc}})}$. This expression for D_B is derived by mapping the bundle to a representative cylindrical rod with a diameter D_B , possessing the same length L_0 and volume as the bundle. This mapping is reasonable when $L_0 \gg w$ and $w \geq D$.

It adjusts c_0 to account for the width of the bundle, thereby influencing the broadness of the orientation distribution function (ODF) $\psi(\theta)$. In terms of the ODF, the volume-equivalent rod approximation ($D_B = D\sqrt{(CN_{\text{sc}})}$) also exhibits the best agreement with the self-consistent ODF derived from the full Onsager solution. The nematic order parameter S from the volume-equivalent rod approximation converges most rapidly to the full Onsager solution compared to the cases of the upper and lower bounds for D_B . As expected, $D_B = D$ yields a lower nematic ordering, while $D_B = w$ leads to an overestimated ordering. This indicates that the primary contributor to the local nematic ordering of the phase is the long axis of the bundle, while other intricate features have a lesser impact.

REFERENCES

- R. M. Parker, G. Guidetti, C. A. Williams, T. Zhao, A. Narkevicius, S. Vignolini, and B. Frka-Petesic, “The self-assembly of cellulose nanocrystals: Hierarchical design of visual appearance,” *Adv. Mater.* **30**, 1704477 (2018).
- J.-F. Revol, H. Bradford, J. Giasson, R. Marchessault, and D. Gray, “Helicoidal self-ordering of cellulose microfibrils in aqueous suspension,” *Int. J. Biol. Macromol.* **14**, 170–172 (1992).
- C. Schutz, M. Agthe, A. B. Fall, K. Gordeyeva, V. Guccini, M. Salajková, T. S. Plivelic, J. P. Lagerwall, G. Salazar-Alvarez, and L. Bergstrom, “Rod packing

in chiral nematic cellulose nanocrystal dispersions studied by small-angle x-ray scattering and laser diffraction," *Langmuir* **31**, 6507–6513 (2015).

- ⁴M. S. Reid, M. Villalobos, and E. D. Cranston, "Benchmarking cellulose nanocrystals: From the laboratory to industrial production," *Langmuir* **33**, 1583–1598 (2017).
- ⁵X. M. Dong, T. Kimura, J.-F. Revol, and D. G. Gray, "Effects of ionic strength on the isotropic–chiral nematic phase transition of suspensions of cellulose crystallites," *Langmuir* **12**, 2076–2082 (1996).
- ⁶Y. Ogawa, "Electron microdiffraction reveals the nanoscale twist geometry of cellulose nanocrystals," *Nanoscale* **11**, 21767–21774 (2019).
- ⁷Z. Zhao, O. E. Shklyaev, A. Nili, M. N. A. Mohamed, J. D. Kubicki, V. H. Crespi, and L. Zhong, "Cellulose microfibril twist, mechanics, and implication for cellulose biosynthesis," *J. Phys. Chem. A* **117**, 2580–2589 (2013).
- ⁸M. Chiappini, S. Dussi, B. Frka-Petescic, S. Vignolini, and M. Dijkstra, "Modeling the cholesteric pitch of apolar cellulose nanocrystal suspensions using a chiral hard-bundle model," *J. Chem. Phys.* **156**, 014904 (2022).
- ⁹T. G. Parton, R. M. Parker, G. T. van de Kerkhof, A. Narkevicius, J. S. Haataja, B. Frka-Petescic, and S. Vignolini, "Chiral self-assembly of cellulose nanocrystals is driven by crystallite bundles," *Nat. Commun.* **13**, 2657 (2022).
- ¹⁰S. Belli, S. Dussi, M. Dijkstra, and R. van Roij, "Density functional theory for chiral nematic liquid crystals," *Phys. Rev. E* **90**, 020503 (2014).
- ¹¹S. Dussi, S. Belli, R. Van Roij, and M. Dijkstra, "Cholesterics of colloidal helices: Predicting the macroscopic pitch from the particle shape and thermodynamic state," *J. Chem. Phys.* **142**, 074905 (2015).
- ¹²S. Dussi and M. Dijkstra, "Entropy-driven formation of chiral nematic phases by computer simulations," *Nat. Commun.* **7**, 11175 (2016).
- ¹³J. Parsons, "Nematic ordering in a system of rods," *Phys. Rev. A* **19**, 1225 (1979).
- ¹⁴S.-D. Lee, "A numerical investigation of nematic ordering based on a simple hard-rod model," *J. Chem. Phys.* **87**, 4972–4974 (1987).
- ¹⁵J. P. Straley, "Theory of piezoelectricity in nematic liquid crystals, and of the cholesteric ordering," *Phys. Rev. A* **14**, 1835 (1976).
- ¹⁶H. H. Wensink, "Effect of size polydispersity on the pitch of nanorod cholesterics," *Crystals* **9**, 143 (2019).
- ¹⁷A. Poniewierski and J. Stecki, "Statistical theory of the elastic constants of nematic liquid crystals," *Mol. Phys.* **38**, 1931–1940 (1979).
- ¹⁸A. Poniewierski, R. Holyst *et al.*, "Density-functional theory for systems of hard rods," *Phys. Rev. A* **41**, 6871 (1990).
- ¹⁹T. Odijk, "Theory of lyotropic polymer liquid crystals," *Macromolecules* **19**, 2313–2329 (1986).
- ²⁰H. Wensink and G. Vroege, "Isotropic–nematic phase behavior of length-polydisperse hard rods," *J. Chem. Phys.* **119**, 6868–6882 (2003).
- ²¹L. Onsager, "The effects of shape on the interaction of colloidal particles," *Ann. N. Y. Acad. Sci.* **51**, 627–659 (1949).
- ²²T. Odijk and H. N. Lekkerkerker, "Theory of the isotropic-liquid crystal phase separation for a solution of bidisperse rodlike macromolecules," *J. Phys. Chem.* **89**, 2090–2096 (1985).
- ²³B. Frka-Petescic, H. Radavidson, B. Jean, and L. Heux, "Dynamically controlled iridescence of cholesteric cellulose nanocrystal suspensions using electric fields," *Adv. Mater.* **29**(11), 1606208 (2017).
- ²⁴J. Straley, "Frank elastic constants of the hard-rod liquid crystal," *Phys. Rev. A* **8**, 2181 (1973).
- ²⁵C. Honorato-Rios and J. P. Lagerwall, "Interrogating helical nanorod self-assembly with fractionated cellulose nanocrystal suspensions," *Commun. Mater.* **1**, 69 (2020).
- ²⁶A. Stukowski, *Modell. Simul. Mater. Sci. Eng.* **18**, 015012 (2010).